Microscopy

Journal of Microscopy, Vol. 258, Issue 3 2015, pp. 241–252 doi: 10.1111/jmi.12238
Received 27 November 2014; accepted 3 February 2015

A fast experimental beam hardening correction method for accurate bone mineral measurements in 3D μCT imaging system

KHODOR KOUBAR*,†, VIRGILE BEKAERT*,†, DAVID BRASSE*,† & PATRICE LAQUERRIERE*,†
*Université de Strasbourg, IPHC, Strasbourg, France
†CNRS, UMR7178, Strasbourg, France

Key words. Artefacts, beam hardening correction, bone mass measurements, preclinical micro-CT.

Summary

Bone mineral density plays an important role in the determination of bone strength and fracture risks. Consequently, it is very important to obtain accurate bone mineral density measurements. The microcomputerized tomography system provides 3D information about the architectural properties of bone. Quantitative analysis accuracy is decreased by the presence of artefacts in the reconstructed images, mainly due to beam hardening artefacts (such as cupping artefacts). In this paper, we introduced a new beam hardening correction method based on a postreconstruction technique performed with the use of off-line water and bone linearization curves experimentally calculated aiming to take into account the nonhomogeneity in the scanned animal. In order to evaluate the mass correction rate, calibration line has been carried out to convert the reconstructed linear attenuation coefficient into bone masses. The presented correction method was then applied on a multimaterial cylindrical phantom and on mouse skeleton images. Mass correction rate up to 18% between uncorrected and corrected images were obtained as well as a remarkable improvement of a calculated mouse femur mass has been noticed. Results were also compared to those obtained when using the simple water linearization technique which does not take into account the nonhomogeneity in the object.

Introduction

Bone mineral density (BMD) and bone mineral content measurements are very important in many preclinical and clinical studies (bone diseases, osteoporosis diagnostic). For longitudinal studies, computerized tomography (CT) is preferred to plastic sections (Particelli *et al.*, 2011). There are many nondestructive methods to measure the BMD and bone mineral content such as the quantitative ultrasound method and the X-ray-based imaging techniques. The quantitative ultrasound is inexpensive, transportable, ionizing radiation-free and can predict fractures risks (Karlsson *et al.*, 2001). But its use is very limited due to some uncertainties concerning its long-term stability, and precision issues. The other methodologies are based on the X-ray imaging such as the dual-energy X-ray absorptiometry (;Genant *et al.*, 1993; Bolotin, 2007), the dual photon absorptiometry (Gotfredsen *et al.*, 1989), the peripheral dual-energy X-ray absorptiometry (Miller *et al.*, 2002), the peripheral quantitative CT (Gasser, 2003) and the micro-CT (μCT) (Brasse *et al.*, 2005; Habold *et al.*, 2011). Dual-energy X-ray absorptiometry cannot assess the measurements in three dimensions from the scan, but it is still considered as a fairly accurate method to measure the BMD. Whereas peripheral quantitative CT can account for the three-dimensional structure of bone but its relative low resolution limits its use especially in small animal scanning. μCT is considered to be the best technique in term of resolution and the three-dimensionality of the bone architecture (Jiang *et al.*, 2000). It is already used to evaluate bone porosity (Britz *et al.*, 2010). Rapidly, it consists in the use of a continuous X-ray spectrum to generate projections of the imaged animal, which will be treated by a reconstruction algorithm to produce a spatial cartography of the linear attenuation coefficient in the animal.

Due to the polychromatic nature of the X-rays spectrum, the attenuation coefficient does not change linearly with the propagation path in the scanned object which leads to a change in the densities in the μCT reconstructed image. This effect is called beam hardening and can degrade the image quality and induce many artefacts such as cupping and streak lines between dense regions. This can affect the linear attenuation coefficient values in the reconstructed image and leads to errors in the BMD and bone mineral content measurements of many quantitative studies (Mulder *et al.*, 2004; Wong *et al.*, 2004; Willmott *et al.*, 2007) where no beam hardening correction methods have been applied.

Many correction methods are proposed to correct the beam hardening artefacts such as the prefiltering, the linearization,

Correspondence to: Patrice Laquerriere, 23 rue du Loess, 67037 Strasbourg, France. Tel: +33 3 88 10 65 09; fax: +33 3 88 10 62 73; e-mail: patrice.laquerriere@iphc.cnrs.fr

the dual energy, the postreconstruction and the iterative correction methods:

(1) The prefiltering (Krimmel *et al.*, 2005; Meganck *et al.*, 2009) is based on the use of filters between the source and the object in order to harden the X-ray spectrum. This method does not eliminate completely the beam hardening artefacts.
(2) The linearization methods (Herman, 1979; Hammersberg & Mangard, 1998; Kachelriess *et al.*, 2006) are based on the estimation of the relationship between the attenuated intensity of the polychromatic source spectrum and the propagation path in the object which can be used to correct the polychromatic data into monochromatic data. This method shows good results for monomaterial objects.
(3) The dual-energy (Lehmann *et al.*, 1981; Remeysen & Swennen, 2006) approach uses two energy levels (two different tube voltages). It increases the dose to the patient (or animal) and needs to cover a wide energy range with the two measurements which becomes difficult in case of multimaterial object.
(4) The postreconstruction method (Nalcioglu & Lou, 1979; Olson *et al.*, 1981) is based on the generation of the projections using the reconstructed image and correcting the polychromatic projections to monochromatic projections. This method requires the knowledge of the energy distribution of the spectrum and the material characteristics.

Recently, Krumm *et al.* (2008) proposed a beam hardening correction method that combines the linearization to a postreconstruction technique where the knowledge of the X-ray spectrum and the physical characteristics of the object materials are not required. Among the iterative methods (Kyriakou *et al.*, 2010; Van Gompel *et al.*, 2011), a new method has been proposed (Yang *et al.*, 2013), which takes into account the nonhomogeneity in the scanned object but requires the knowledge of the materials density (that is not our case). This method requires a set of projections and reprojections in order to obtain the corrected reconstructed image. Van Gompel *et al.* (2011) have also recently proposed an iterative method aiming to improve the calculation of the distances crossed by the X-rays into each material by simulating the polychromatic and the monochromatic projections with the use of a ray tracing algorithm in order to add to the measured data the difference between the two simulated intensities. However, the obtained reconstructed values have no physical meaning. In addition, in most of the cited papers, no validation of the various methods on a real sample (like a mouse for bone measurement) has been done.

In this study, since the scanned animal tissues are known, we proposed to perform the attenuation curves for the soft tissue and for bone experimentally and to use them for correcting the measured projections for each tissue. This is a major difference with Krumm *et al.* (2008) study which is based on an inline determination of the monochromatic data. The calculation of the distances crossed by the X-rays in each material is done through a ray tracing algorithm. In this paper, we introduce a fast experimental beam hardening correction method in order to show the effect of its application on the values of the reconstructed linear attenuation coefficient of bone and consequently on bone masses. The present method is a combination of an off-line linearization technique and postreconstruction method that does not need any prior knowledge about the X-ray spectrum (Koubar *et al.*, 2011), which is the case in the postreconstruction processes and which can introduce errors to the applied correction values. In the first part, we explain the principles of the linearization technique combined to the postreconstruction process which takes into account the nonhomogeneity in the imaged animal. In addition, we validate our correction method by applying it on a multimaterial object and on small animal (mouse skull and femur). In the last part we show how the presented correction method affects the bone linear attenuation coefficient and thereby lead to more accurate BMD and bone mineral content measurements on mouse bones. Comparisons with results obtained when using an already existed water linearization technique are also discussed.

Materials and methods

The μCT system

The cone beam μCT system has been constructed at the IPHC (Institut Pluridisciplinaire Hubert Curien), Strasbourg, France. This system has previously been described (Brasse *et al.*, 2005). It consists of an X-ray source, an X-ray detector and 3D translation and rotation stages. The X-ray source is a commercially sealed tube (L9181-02, Hamamatsu) with a tungsten anode, a 200 μm beryllium and a 1-mm aluminium exit windows. The source has an 8 μm focal spot and a maximum output power of 8 W. With a selected output power less than 4 W, the size of the focal spot is 5 μm. The X-ray source operates in continuous mode with a 39° maximum beam angle. The X-ray detector is a commercially available flat panel sensor (C7942CA-22, Hamamatsu) composed of a CsI scintillator plate coupled to 1-mm aluminium filter and a two-dimensional photodiode array Complementary Metal Oxide Semiconductor (CMOS) leading to an active area of 120×120 mm^2 and 2400×2400 active pixel elements. The pixel size is 50×50 μm^2. Due to diffusion, the intrinsic resolution is around 75 μm. Due to the zoom effect, the spatial resolution is 50 μm. Our measurements were acquired with a 40 kV source voltage and an anode current of 200 μA (maximum voltage value for this source: 130 kV corresponding to a current of 300 μA). The acquisition parameters have been chosen to insure a compromise between a good contrast and a low

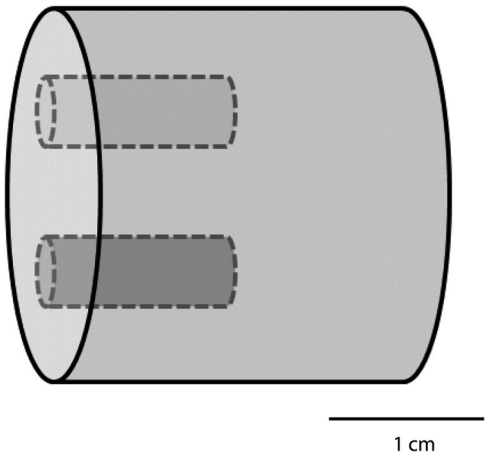

Fig. 1. Illustration of the cylindrical phantom.

dose taking into account the scanned animal size (Grodzins, 1983).

Phantom description

The phantom used is an empty cylinder containing two other small cylinders as shown in Figure 1. This phantom helps to test the validity of the presented correction method in case of multimaterial object (water–air–bone) and its contribution in term of contrast and cupping artefact corrections. In order to have a three-material object, we filled one of the small cylinders with the hydroxyapatite (HA) powder $Ca_{10}(PO_4)_6(OH)_2$ (HA) which is a major component of bone and represents more than 70% of bone's chemical composition. Similarly, the second small cylinder is filled with water.

The origin of the beam hardening

Let us consider a monochromatic source of X-rays with a single energy E. For a given pixel in the detector, using the beer's law the monochromatic projection is given by:

$$P_m = -\mathrm{IN}\left(\frac{\mathrm{I_m} - \mathrm{I_B}}{\mathrm{I_{m0}} - \mathrm{I_B}}\right) = \int_{-\infty}^{+\infty} \mu(\mathrm{x,y})\mathrm{dl}, \tag{1}$$

where I_{m0} is the intensity of the source measured by the detector, I_m is the attenuated one after crossing a distance l through the object, I_B is the noise and μ is the attenuation coefficient at the position $(x; y)$ for the energy E. In our case, the spectrum used in μCT is polychromatic. This means that the polychromatic projection can be expressed by:

$$\begin{aligned} P_p &= -\mathrm{In}\left(\frac{\mathrm{I_p} - \mathrm{I_B}}{\mathrm{I_{p0}} - \mathrm{I_B}}\right) \\ &= -\mathrm{In}\left(\frac{\int_0^{\mathrm{E_{max}}} \mathrm{S(E)D(E)}exp(-\int_{-\infty}^{+\infty} \mu(\mathrm{x,y,E})\mathrm{dl})\mathrm{dE} - \mathrm{I_B}}{\int_0^{\mathrm{E_{max}}} \mathrm{S(E)D(E)dE} - \mathrm{I_B}}\right), \end{aligned} \tag{2}$$

where Ip_0 is the polychromatic spectrum intensity, Ip is the attenuated one, $S(E)$ represents the X-rays spectrum and $D(E)$ is the detector efficiency.

We can notice that Eq. (1) shows a linear relationship between the monochromatic projection and the distance crossed by the X-rays in the object whereas it is not the case in Eq. (2). Since the X-rays are considered as monochromatic in the μCT reconstruction, we have to correct the nonlinear data into linear data in order to decrease the beam hardening artefacts. This method is called the linearization.

The proposed method

Correction procedure. Figure 2 shows the flow chart of the presented beam hardening correction method. It has been implemented with C++. A first reconstructed image is performed in order to threshold the different materials: air, water and bone. Off-line water and bone attenuation curves are then used to correct the pixels values of each projection depending on the propagation path lengths of the X-rays in each material. A first segmentation step of the image has to be done using global thresholds. The propagation path lengths are then calculated via a ray tracing algorithm which provides information about the voxel values and the distances crossed by the X-ray within the voxel along the X-ray path from the source to the considered pixel. This study has to be done for each pixel of each projection. The projection value of the pixel $(i; j)$ can be expressed by:

$$P_p(i,\ j) = \sum_{k=0}^{N_{\max}} P_{pk}(i,\ j), \tag{3}$$

where $N_{\max}$ is the number of materials in the object. In our case, $N_{\max}$ is equal to 3, and the segmentation thresholds are set to distinguish air, water (soft tissue) and bone. The propagation values of each material are then normalized in order to obtain their sum equal to the experimental projection value.

Since our proposed method is based on the use of attenuation curves in order to linearize the measured data, we present first, in section 'The attenuation curves' our linearization procedure used during our correction procedure.

The attenuation curves. Water and bone attenuation curves have to be done by measuring the total detected signal in the detector each time we increase the material's thickness crossed by the X-ray beam for each pixel. A sufficient third-degree polynomial (Hammersberg & Mangard, 1998) has been chosen to fit the distance crossed by the X-rays d as a function of the polychromatic projections P_p as shown in the following equation:

$$d = a.Pp + b.P_p^2 + c.P_p^3, \tag{4}$$

where a, b and c are the polynomial parameters. Each point of this polynomial should be corrected in order to be equal to the

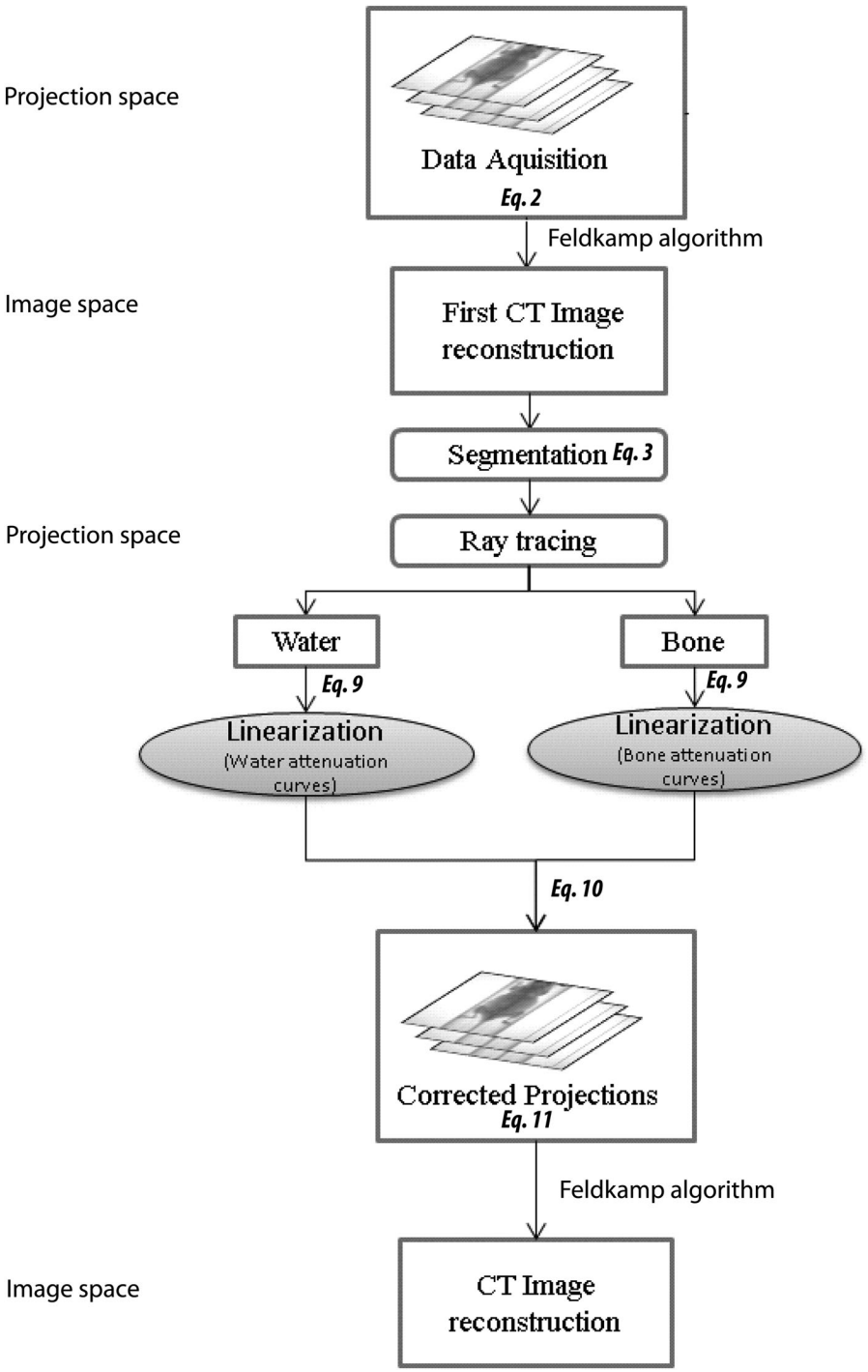

Fig. 2. Flow chart of the two beam hardening correction methods.

data obtained in the case of a monochromatic spectrum where the corresponding monochromatic projection P_m is given by:

$$P_m = -\mathrm{In}\left(\frac{\mathrm{I_m}}{\mathrm{I_{m0}}}\right) = \bar{\mu}.\mathrm{d}, \tag{5}$$

where μ is the material linear attenuation coefficient at the energy of the monochromatic spectrum, I_{m0} is the intensity of the source measured by the detector, I_m is the attenuated one (see Eq. (1) and we can write:

$$d = \frac{1}{\bar{\mu}}.P_m. \tag{6}$$

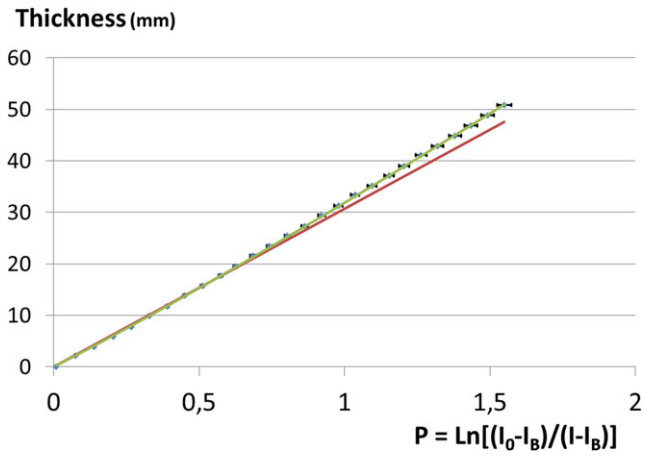

Fig. 3. Projection values as a function of Plexiglas thicknesses. The green curve represents the fitted function of the polychromatic data (blue dots) for a given pixel, and the red line is the corresponding calculated monochromatic data.

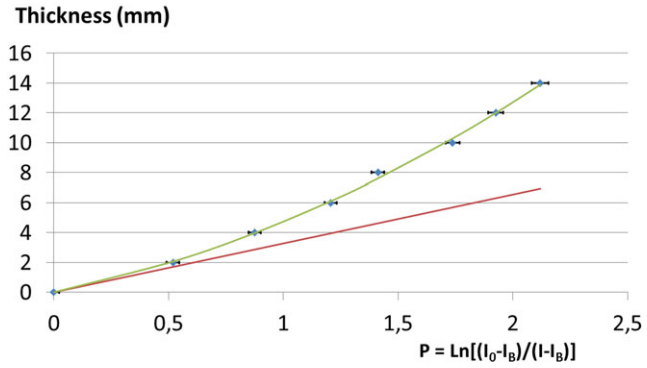

Fig. 4. Projection values as a function of HA powder thicknesses. The green curve represents the fitted function of the mean polychromatic data (blue dots) and the red line is the corresponding calculated monochromatic data.

Using Eqs. (4) and (6), we can write:

$$d = \frac{1}{\mu}.P_m = a.P_p + b.P_P^2 + c.P_P^3. \tag{7}$$

For small distances (when $d \to 0$), the beam hardening effect is negligible which makes $P_m = P_p$, and we can write:

$$\frac{1}{\mu} = a + b.P_p + c.P_p^2, \tag{8}$$

for $d = 0$, $P_m = 0$, we obtain:

$$\frac{1}{\mu} = a. \tag{9}$$

Knowing the value of μ, we can obtain now the monochromatic projections P_m for each thickness of the considered material. The corrected projections could be written as:

$$P_{pcor} = \bar{\mu}[a.P_p + b.P_P^2 + b.P_P^3] = F(P_p), \tag{10}$$

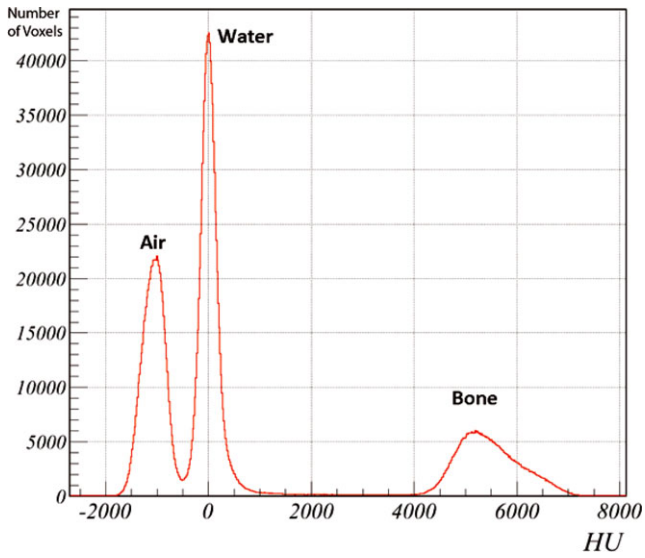

Fig. 5. Greyscale values distribution in the reconstructed image of the cylindrical phantom. HU, Hounsfield Units.

where $F(P_p)$ is the correction operator for each pixel of the detector array. The experimental attenuation coefficient used in the correction equation must be unique for all the detector pixels and will be equal to the inverse of the mean value of the 'a' polynomial coefficients of all the pixels. In our work, we consider that the studied animal contains air (lungs), water (soft tissues) and HA (bone). As the air does not cause beam hardening artefacts, two attenuation curves for water and for bone are carried out to be then used in the correction method. Having very close values of the mass attenuation coefficient, the Plexiglas (1.19 g cm^{-3}) is used to replace the soft tissue (1.06 g cm^{-3}) or water (1 g cm^{-3}). Therefore, the attenuation curves were carried out by the use of 12×12 cm^2 Plexiglas plates whose the combination allows us to have a set of thicknesses between 0 and 50 mm with a step of 2 mm. For the bone attenuation curves, we used HA powder. Due to some technical constraints, the measurements with the HA powder were done only on a limited region of the detector and the measured polychromatic data were averaged for the scanned region for each HA powder thickness (from 0 to 14 mm with a step of 2 mm). It was not a problem since the size of mice bone does not exceed few mm. For both cases, the measured polychromatic data were fitted via the polynomial function in order to obtain the fitting parameters, which will be used in the correction procedure.

Using the attenuation curves of water and bone, the polychromatic projections (P_p)water and (P_p)bone are corrected to (P_{pcor})water and (P_{pcor})bone, respectively as shown in Eq. (9). The corrected projection value of a given pixel $(i; j)$ becomes:

$$P_{pcor}(i, j) = \sum_{k=0}^{N_{max}} P_{pcor}(i, j). \tag{11}$$

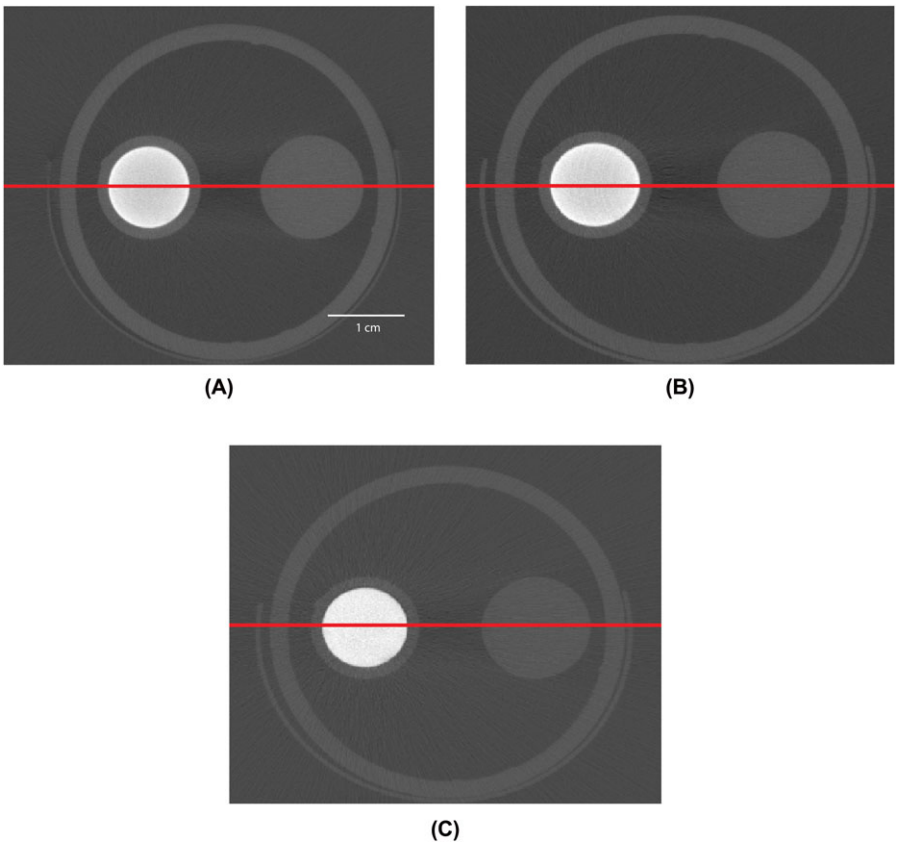

Fig. 6. Axial sections of (A) the uncorrected phantom, (B) the corrected phantom with the water correction and (C) the corrected phantom with the proposed water/bone correction.

Once all the projections are corrected, a second, final reconstruction is done. In the next section, we show results of the simple linearization and presented correction methods when applied on the cylinder described in section 'Phantom description' and on mouse skeleton. In order to evaluate the improvements in the corrected images, we calculated the nonuniformity degree ('cupping degree') $T_{\text{cup}}(\%)$ and the contrast between two regions intensities (I_{bone} and I_{water}) C, which are respectively defined by:

$$T_{cup} = \frac{\mu_{edge} - \mu_{center}}{\mu_{center}} \times 100\,(\%) \tag{12}$$

and

$$C = \frac{I_{bone} - I_{water}}{I_{bone} + I_{water}}, \tag{13}$$

where μ_{edge} and μ_{centre} are the linear attenuation coefficients of the edge and the centre of the cylindrical volume studied, respectively.

Small animal

In order to show how the correction method can affect the linear attenuation coefficient of bone and the mineral bone masses when applied on mouse skeleton and mouse skull and femur, we used a calibration curve to convert the linear attenuation coefficient into bone masses. The calibration line was calculated by measuring the corresponding reconstructed linear attenuation coefficient of a dipotassium phosphate (K2HPO4) solutions of variable known concentrations (Habold *et al.*, 2011). The equation of the conversion line was:

$$y = 2.44x + 0.847, \tag{14}$$

where x represents the linear attenuation coefficient and y, the bone density. The mass correction rate between the corrected (M_{cor}) and the uncorrected mass (M_{unc}) is then calculated and it is given by:

$$\frac{\Delta M}{M} = \frac{M_{unc} - M_{cor}}{M_{unc}} \,.\, 100, \tag{15}$$

where M_{unc} is the bone mass value obtained without Beam Hardening (BH) correction and M_{cor} is the bone mass obtained with our correction method.

The value of the mass correction rate will be an evaluating factor of the underestimation of the calculated bone mass without correction. A higher mass correction rate obtained indicates a more significant underestimation of bone mass.

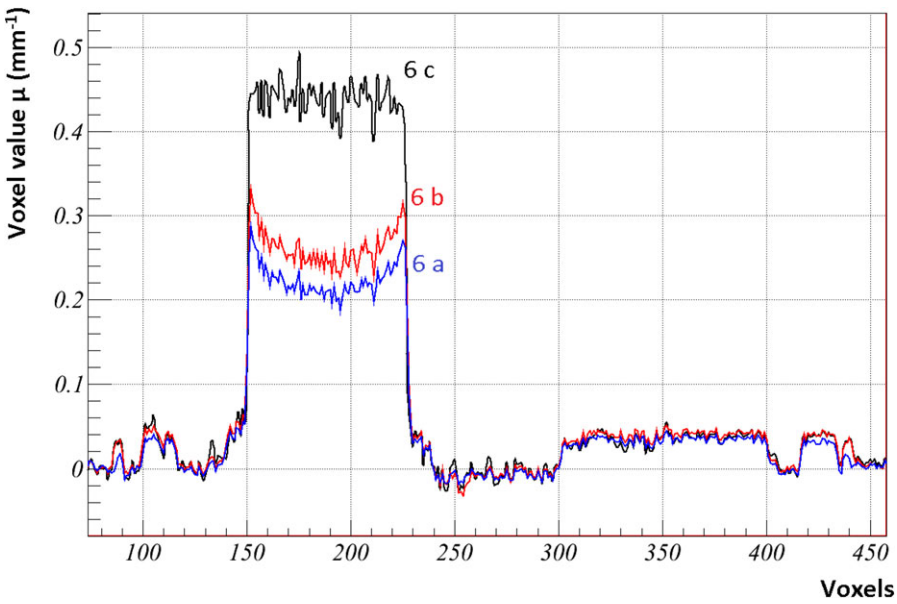

Fig. 7. Central line profile of the uncorrected cylinder (blue line, 6A), corrected cylinder with the water correction (red line, 6B) and corrected cylinder with the proposed water/bone correction (black line, 6C).

Results

The attenuation curves

The fitted mean polychromatic (green curve) and monochromatic data (red line) when using Plexiglas plates and HA powder are plotted in Figures 3 and 4, respectively.

The mean parameters values for the Plexiglas are: $a = 30.62 \pm 0.24$, $b = 3.035 \pm 0.51$ and $c = -0.70 \pm 0.17$. The obtained fitting parameters for the HA powder are: $a = 3.27 \pm 0.04$, $b = 1.43 \pm 0.05$ and $c = 0.06 \pm 0.02$.

Correction procedure

Multimaterial object correction. As shown in Figure 5, the linear attenuation coefficient distribution of the image voxels allows us to determine the thresholds between the three studied materials. Figure 6 shows the cross-sections of the uncorrected cylinder and the corrected cylinders. The central line profiles in Figure 7 shows that the image contrast has increased using the corrections in the bone regions. The cupping artefacts present in the uncorrected image are completely removed with the presented correction method, whereas it is not the case with the water linearization correction. The nonuniformity degree of the attenuation coefficient of bone decreases widely from around $35.20 \pm 4.4\%$ in the uncorrected bone region to $3.12 \pm 3.56\%$ when using our proposed correction method of the same region, whereas it remains high with the water linearization correction with a value of $30.64 \pm 4.15\%$.

BMD evaluation in small animal. Figure 8 shows the axial sections of an uncorrected mouse skeleton image and corrected images. The corresponding linear attenuation coefficient profiles along the red line are shown in Figure 9. The contrast between the bone and the neighbouring region along the red line has increased when applying the correction methods: (i) without correction: $C = 0.526$, (ii) water linearization correction: $C = 0.619$, (iii) the proposed correction method: $C = 0.652$. After defining a threshold to take into consideration the bone zones only, the masses of the uncorrected and the corrected images are then calculated and the correction rate distributions are given in Figure 10. The mean value of the bone mass correction rate has increased with the proposed correction method. Furthermore, the corresponding correction distribution is wider and reaches values up to 15%, whereas the maximum values reached when using the water linearization correction were around 6%. In order to visualize the difference between the correction rate of both methods, and since only around $3.0 \pm 1.2\%$ of the image voxels were corrected with values above 10%, we set the scale of the correction rate from 0% to 10%. Figures 11(A)–(F) show that the axial, coronal and sagittal slices of the mass correction rate of a mouse skeleton obtained with both correction methods. Then, it has to be demonstrated that the mass correction rate is not affected by the cone beam geometry and the Feldkamp reconstruction algorithm used. For this goal, we imaged a homogeneous cylinder containing HA powder. A uniform correction rate of powder mass was obtained, (see Fig. 12).

Finally, we validated our proposed correction method on mice bone measurements. Using the conversion line between

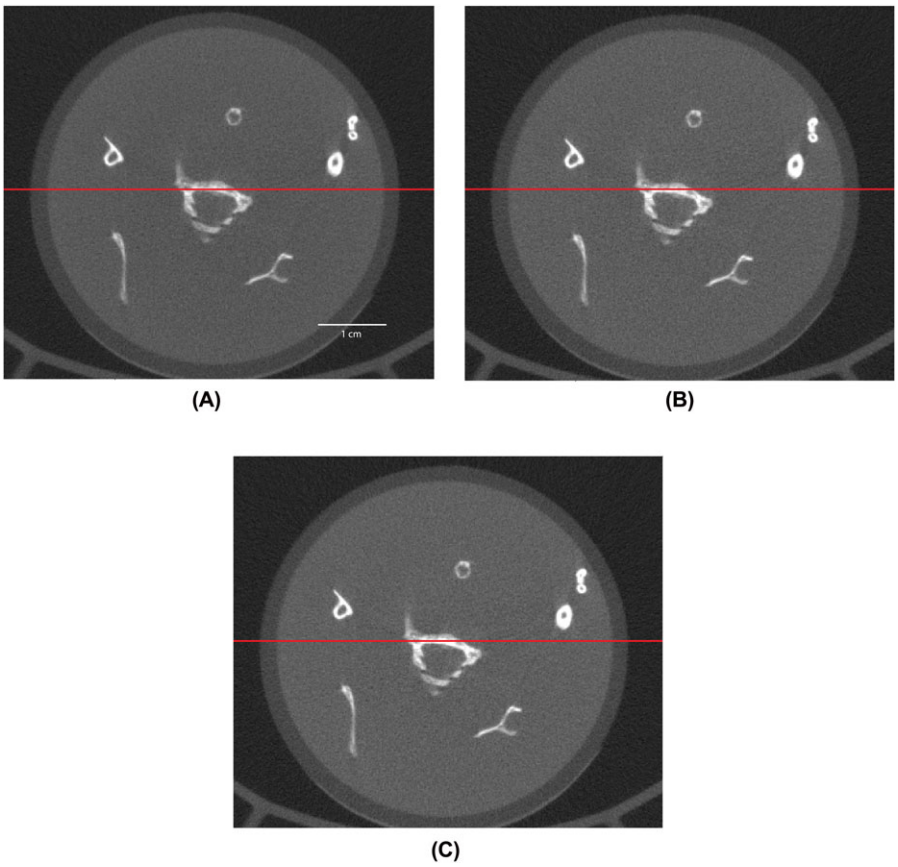

Fig. 8. Axial sections of (A) uncorrected mouse skeleton image, and (B) the corrected ones using the water correction method and (C) the proposed water/bone correction method.

Table 1. Measured and calculated bone mass of a femur and skull.

		Without BH correction		With BH correction	
	Measured weight (mg)	Calculated weight (mg)	Relative error	Calculated weight (mg)	Relative error
Femora along rotation axis		116.01 ± 0.09	+5.1%	110.36 ± 0.14	+0.0%
Femora perpendicular to rotation axis	110.35 ± 0.27	104.68 ± 0.02	−5.1%	110.30 ± 0.15	−0.0%
Femora random position		112.85 ± 0.06	+2.2%	110.70 ± 0.19	+0.3%
skull	674.20 ± 0.30	724.02 ± 0.24	+7.3%	651.71 ± 0.30	−3.4%

the reconstructed values of the linear attenuation coefficient of bone and bone density (Eq. (12)), we calculated the mass of a mouse femur and skull through uncorrected and corrected images. The exact weight of the dried femur was 110.3 ± 0.3 mg. When the femur was positioned along the rotation axis of the μCT, the values we obtained without correction and with the proposed correction method are 116.0 ± 0.1 mg and 110.4 ± 0.1 mg, respectively (Table 1). The coronal section of the mass correction rate of femur with the proposed correction method reached values up to 20% have been observed. When the femur was positioned perpendicular the rotation axis of the μCT, the calculated mass were 104.7 ± 0.1 mg and 110.3 ± 0.2 mg, without or with correction, respectively. When there was a random angle between the femur and the rotation axis of the μCT, the mass calculated were 112.9 ± 0.1 mg and 110.7 ± 0.2 mg without and with correction. Finally, we weighted a dry skull and obtained 674.2 ± 0.3 mg. the calculated mass were 724.0 ± 0.1 and 651.7 ± 0.3 mg, without or with correction, respectively

Discussion

The uniform correction rate obtained in the case of the homogeneous cylinder proves the independence of the reconstructed voxel value from the dedicated cone beam Feldkamp reconstruction algorithm. Iterations cannot be performed in

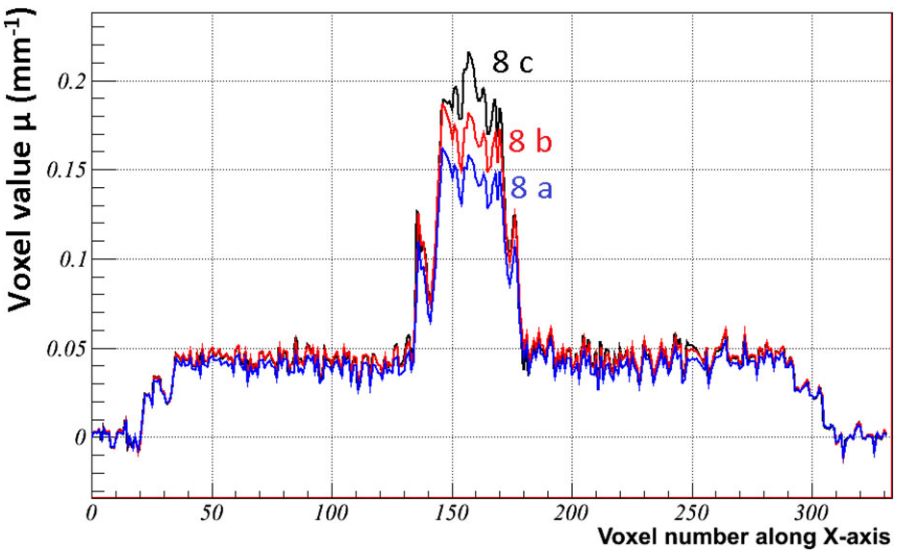

Fig. 9. Line profile of the uncorrected mouse skeleton image (blue line, 8A), the corrected one with the water correction (red line, 8B) and the corrected one with the proposed bone/water correction (black line, 8C). The pixel size is 100 μm.

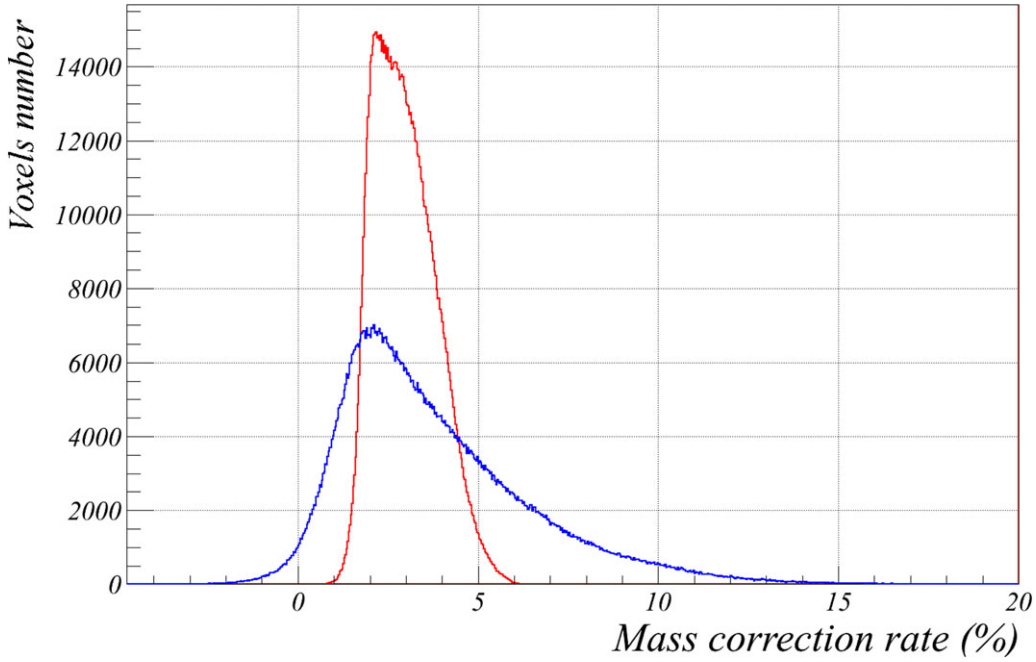

Fig. 10. Distributions of bone mass correction rate with the water correction method (red curve) and the proposed bone/water correction method (blue curve).

this method because the corrected values are obtained directly after the first experimental linearization. Otherwise greater corrected values will be obtained and no convergence is reached (data not shown). For this reason, the experimental attenuation curves have to be done carefully for each material. A generally common problem that faces this method is the truncation data which can introduce an enormous error on the calculated projections. To overcome this constraint, limited region of interests are selected where no truncated values exists.

Since the attenuation curves were done experimentally and off-line, the presented method is considered to be very fast (17 s per projection on a single 2.67 GHz Xeon CPU) in comparison to others methods where the linearization are done in-line and during the correction procedure (Krumm *et al.*, 2008) or where a set of projections and reprojections are

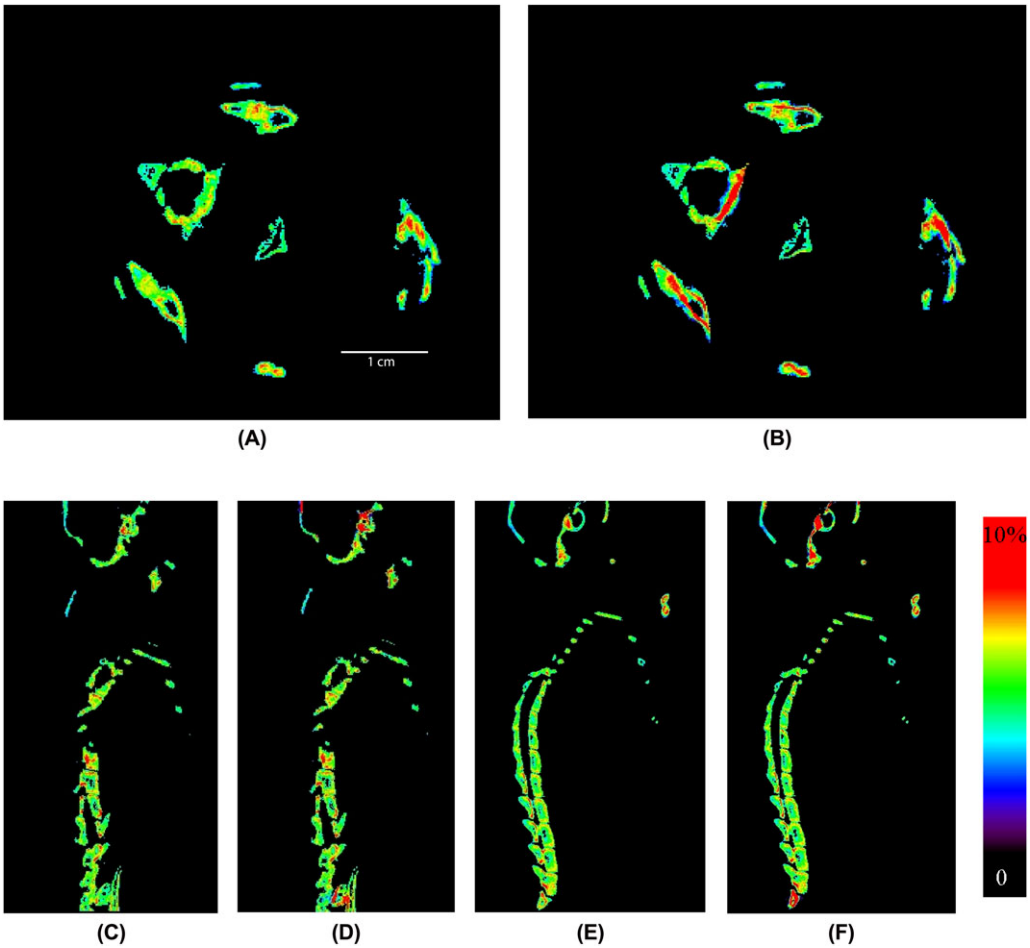

Fig. 11. Axial, coronal and sagittal slices of the mass correction rate of a mouse skeleton obtained by the water correction method (A), (C), (E) and by the proposed water/bone correction method (B), (D), (F) in the same scale.

required and performed iteratively (Kyriakou *et al.*, 2010). One disadvantage of the presented method is the calculation of the projections through an uncorrected image which can introduce errors especially when severe artefacts appear. This is not the case when small animal-like mice are used. A scatter correction would be helpful in order to obtain scatter-corrected μCT values which can reduce the errors on the calculated projections through a first scatter-corrected image.

Due to the water abundance in the mouse's body and the small thicknesses of bone crossed by the X-rays, no severe streak line artefacts are observed in the preclinical images obtained. In addition, the chosen third polynomial degree seems to be sufficient to fit the measured data. The nonlinear behaviour of the attenuation curves obtained in the previous section show that the beam hardening effect is more important with bone than with soft tissue. This is normal and expected due to the higher attenuation coefficient values of the HA powder than those of Plexiglas. Originally, methods included also fat correction (Ruegsegger *et al.*, 1978). Since our X-ray source contains a 1 mm Al window, the water and fat corrections were not very useful. Once these off-line attenuation curves are done, the segmentation thresholds are set to separate the present materials in the phantom or in the animal by analysing the distribution of the greyscale values. The obtained profiles in both cases (the phantom and the mouse skeleton) show that the water linear attenuation coefficient does not change with the correction methods. This can be explained by the quasilinear behaviour of the water attenuation curves which it is not the case with the HA curves. Consequently, the contrast has increased with the two correction methods. However, the cupping artefacts in the bone region of the cylindrical phantom is not removed using the water linearization correction method, while it is the case with the proposed correction method. In addition, the correction rate is not uniform and differs from region to another in the mouse skeleton depending on the thicknesses and the densities of the corresponding bones. The amount of the corrected bone voxels by the water/bone correction in the whole skeleton image where the mass correction rate is greater than 5%, represents around $34.60 \pm 8.68\%$ of the total bone voxels number and

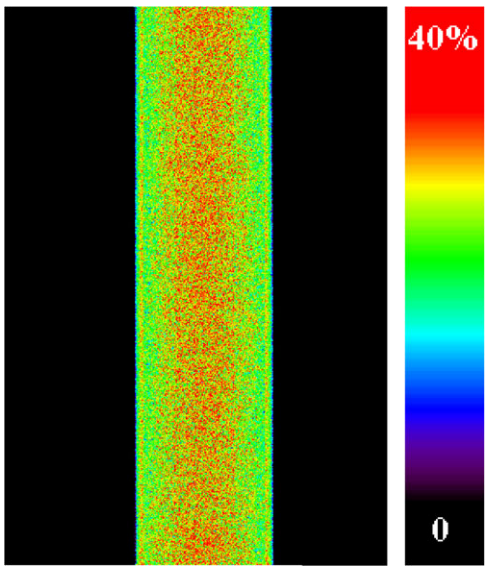

Fig. 12. Correction rate of a reconstructed axial slice of a homogeneous cylinder containing HA powder. (Slice dimensions: 512×720 voxels with a voxel size of $0.1 \times 0.1 \times 0.1$ mm^3.)

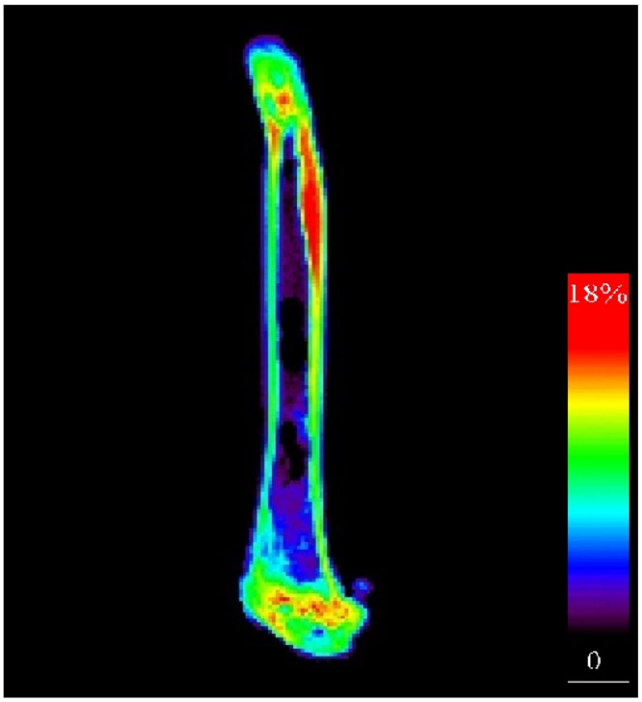

Fig. 13. Example of mass correction rate of mouse femur using the proposed water/bone correction method.

it can reach greater values when selecting a single slice. This high percentage has to be taken into account in the determination of the mineral bone masses. Otherwise, the errors introduced in the mass bone calculations will be very important and this will lead to false bone mineral measurements. In this work, we calculated the total bone mass of a skeleton but the obtained value was lower than the measured weight. This may be due to the difficulty to remove 100% of the soft tissue from the skeleton. Furthermore, the attenuation curves are done usually with a constant density material which it is not the case of skeleton where the BMD is not uniform and varies from region to another. In the case of isolated bones (femur or skull) the mass calculation was very good after beam hardening correction. In mean, the relative error on the weight was 0.1% for the three positions of the femur. At the opposite, without beam hardening correction, the relative error was between −5% and + 5, in function of the position (Figure 13). This means that, without correction, when the X-rays cross a small amount of bone (femur along the rotation axis) the mass is overestimated. When X-rays cross longer distances of bone (femur perpendicular to the rotation axis) the calculated mass was underestimated (even if the distances crossed are heterogeneous). When a skull was used, the corrected calculated mass was underestimated (3.4%). But since it is almost impossible to remove all the soft tissue from the skull it is more likely that the calculated mass is correct but the measured mass is not correct. This deviation from the 'real' value may also be due to the uncorrected scatter signal present in the projections even if the correction is weak in the case of bones. But, in our case, the beam hardening correction was almost enough, we did not need to compensate by a function (Hewei *et al.*, 2006).

Conclusions

In this paper, we showed that our beam hardening correction method based on bone linearization in μCT can widely reduce the beam hardening artefacts when taking into account the nonhomogeneity in the scanned animal and can also correct the reconstructed linear attenuation coefficient values, especially for the bone without any prior knowledge about the X-ray spectrum. One important step in our presented method is the determination of the thresholds that separates between materials in order to correct each voxel value in the image by the use of the off-line attenuation curves and its corresponding correction line. We showed also that applying our proposed correction method on animal isolated bones images leads to greater mass correction rates than the case of the simple water linearization method, which allows us to reach an accurate bone mass measurement. The proposed method allowed us to obtain the exact mass of a bone whatever was the distance crossed by the X-rays.

References

Brasse, D., Humbert, B., Mathelin, C., Rio, M.C. & Guyonnet, J.L. (2005) Towards an inline reconstruction architecture for micro-CT systems. *Phys. Med. Biol.* **50**, 5799–5811.

Britz, H.M., Jokihaara, J., Leppänen, O.V., Järvinen, T. & Cooper, D.M. (2010) 3D visualization and quantification of rat cortical bone porosity

using a desktop micro-CT system: a case study in the tibia. *J. Microsc.* **240**(1), 32–37.

Bolotin, H. (2007) DXA in vivo BMD methodology: an erroneous and misleading research and clinical gauge of bone mineral status, bone fragility, and bone remodelling. *Bone* **41**, 138–154.

Gasser, J.A. (2003) Bone measurements by peripheral quantitative computed tomography in rodents methods in molecular medicine. **80**, 323-341.

Genant, H.K., Faulkner, K.G., Glüer, C.C. & Engelke, K. (1993) Bone densitometry: current assessment. *Osteoporos. Int.* **3**, 91–97.

Gotfredsen, A., Podenphant, J., Nilas, L. & Christiansen, C. (1989) Discriminative ability of total body bone-mineral measured by dual photon absorptiometry. *Scand. J. Clin. Lab. Invest.* **49**, 125–134.

Grodzins, L. (1983) Optimum energies for x-ray transmission tomography of small samples: applications of synchrotron radiation to computerized tomography I. *Nucl. Instrum. Methods Phys. Res.* **206**, 541–545.

Habold, C., Momken, I., Ouadi, A., Bekaert, V. & Brasse, D. (2011) Effect of prior treatment with resveratrol on density and structure of rat long bones under tail-suspension. *J. Bone Miner. Metab.* **29**, 15–22.

Hammersberg, P. & Mangard, M. (1998) Correction for beam hardening artefacts in computerized tomography. *J. X-ray Sci. Technol.* **8**, 75–93.

Herman, G.T. (1979) Correction for beam hardening in computed tomography. *Phys. Med. Biol.* **24**, 81–106.

Hewei, G., Li, Z., Chen, Z., Yuxiang, X. & Shuanglei, L. (2006) Beam hardening correction for middle-energy industrial computerized tomography. *IEEE-TNS* **53**(5), 2796–2807.

Jiang, Y., Zhao, J., White, D.L. & Genant, H.K. (2000) Micro CT and micro MR imaging of 3D architecture of animal skeleton. *Musculoskelet. Neuronal. Interact.* **1**, 45–51.

Kachelriess, M., Sourbelle, K. & Kalender, W.A. (2006) Empirical cupping correction: a first-order raw data precorrection for cone-beam computed tomography. *Med. Phys.* **33**, 1269–1274.

Karlsson, M., Duan, Y., Ahlborg, H., Obrant, K., Johnell, O. & Seeman, E. (2001) Age, gender and fragility fractures are associated with differences in quantitative ultrasound independent of bone mineral density. *Bone* **28**, 118–122.

Koubar, K., Vintache, D., El Bitar, Z., Laquerriere, P. & Brasse, D. (2011) Analytical simulation of a microCT system in computed tomography. Fully three-dimensional image reconstruction in radiology and nuclear medicine (Fully3D). 214–217.

Krimmel, S., Stephan, J. & Baumann, J. (2005) 3D computed tomography using a microfocus X-ray source: Analysis of artifact formation in the reconstructed images using simulated as well as experimental projection data. *Nucl. Instrum. Methods Phys. Res. A.* **542**, 399–407.

Krumm, M., Kasperl, S. & Franz, M. (2008) Reducing non-linear artifacts of multi-material objects in industrial 3D computed tomography International. *J. Coal Geol.* **41**, 242–251.

Kyriakou, Y., Meyer, E., Prell, D. & Kachelriess, M. (2010) Empirical beam hardening correction (EBHC) for CT. *Med. Phys.* **37**, 5179–5187.

Lehmann, L.A., Alvarez, R.E., Macovski, A., Brody, W.R., Pelc, N.J., Riederer, S.J. & Hall, A.L. (1981) Generalized image combinations in dual KVP digital radiography. *Med. Phys.* **8**, 659–667.

Meganck, J.A., Kozloff, K.M., Thornton, M.M., Broski, S.M. & Goldstein, S.A. (2009) Beam hardening artifacts in micro-computed tomography scanning can be reduced by X-ray beam filtration and the resulting images can be used to accurately measure. *BMD Bone* **45**, 1104–1116.

Miller, P.D., Siris, E.S., Barrett-Connor, E., *et al.* (2002) Prediction of fracture risk in postmenopausal white women with peripheral bone densitometry: evidence from the National Osteoporosis Risk Assessment. *J. Bone Miner. Res.* **17**, 2222–2230.

Mulder, L., Koolstra, J.H. & Van Eijden, T.M. (2004) Accuracy of microCT in the quantitative determination of the degree and distribution of mineralization in developing bone. *Acta Radiol.* **45**, 769–777.

Nalcioglu, O. & Lou, R.Y. (1979) Post-reconstruction method for beam hardening in computerized tomography. *Phys. Med. Biol.* **24**, 330–340.

Particelli, F., Mecozzi, L., Beraudi, A., Montesi, M., Baruffaldi, F. & Viceconti, M. (2011) A comparison between micro-CT and histology for the evaluation of cortical bone: effect of polymethylmethacrylate embedding on structural parameters. *J. Microsc.* **245**(3), 302–310.

Olson, E.A., Han, K.S. & Pisano, D.J. (1981) CT reprojection polychromaticity correction for three attenuators. *IEEE Trans. Nucl. Sci.* **28**, 3628–3640.

Remeysen, K. & Swennen, R. (2006) Beam hardening artifact reduction in microfocus computed tomography for improved quantitative coal characterization. *Int. J. Coal Geol.* **67**, 101–111.

Ruegsegger, P., Hangartner, T., Keller, H.U. & Hinderling, T. (1978) Standardization of computed tomography Images by means of a material-selective beam hardening correction. *J. Comput. Ass. Tomogr.* **2**, 184–188.

Van Gompel, G., Van Slambrouck, K., Defrise, M., Batenburg, K.J., de Mey, J., Sijbers, J. & Nuyts, J. (2011) Iterative correction of beam hardening artifacts in CT. *Med. Phys.* **38**, S36–S49.

Willmott, N.S., Wong, F.S. & Davis, G.R. (2007) An X-ray microtomography study on the mineral concentration of carious dentine removed during cavity preparation in deciduous molars. *Caries Res.* **41**, 129–134.

Wong, F.S., Anderson, P., Fan, H. & Davis, G.R. (2004) X-ray microtomographic study of mineral concentration distribution in deciduous enamel. *Arch. Oral Biol.* **49**, 937–944.

Yang, Q., Maass, N., Tian, M., Elter, M., Schasiepen, I., Maier, A. & Hornegger, J. (2013) Multi-Material Beam Hardening Correction (MMBHC) in computed tomography. Fully three-dimensional image reconstruction in radiology and nuclear medicine (Fully3D). 533–536.